Society For Biomaterials

Degradable magnesium-based implant materials with anti-inflammatory activity

Qiuming Peng,[1] Kun Li,[1] Zengsheng Han,[1] Erde Wang,[2] Zhigang Xu,[3] Riping Liu,[1] Yongjun Tian[1]

[1]State Key Laboratory of Metastable Materials Science and Technology, Yanshan University, Qinhuangdao, 066004, People's Republic of China
[2]School of Materials Science and Engineering, Harbin Institute of Technology, Harbin 150001, People's Republic of China
[3]NSF Engineering Research Center for Revolutionizing Metallic Biomaterials, Suite #105, Fort IRC Building, 1601 East Market Street, North Carolina

Received 20 April 2012; revised 23 October 2012; accepted 23 October 2012
Published online 3 December 2012 in Wiley Online Library (wileyonlinelibrary.com). DOI: 10.1002/jbm.a.34494

Abstract: The objective of this study was to prepare a new biodegradable Mg-based biomaterial, which provides good mechanical integrity in combination with anti-inflammatory function during the degradation process. The silver element was used, because it improved the mechanical properties as an effective grain refiner and it is also treated as a potential anti-inflammatory core. The new degradable Mg-Zn-Ag biomaterial was prepared by zone solidification technology and extrusion. The mechanical properties were mostly enhanced by fine grain strengthening. In addition, the alloys exhibited good cytocompatibility. The anti-inflammatory function of degradation products was identified by both interleukin-1α and nitric oxide modes. The anti-inflammatory impact was significantly associated with the concentration of silver ion. It was demonstrated that Mg-Zn-Ag system was a potential metallic stent with anti-inflammatory function, which can reduce the long-term dependence of anti-inflammatory drug after coronary stent implantation. © 2012 Wiley Periodicals, Inc. J Biomed Mater Res Part A: 101A: 1898–1906, 2013.

Key Words: metallic implant, mechanical properties, degradation properties, anti-inflammatory activity

How to cite this article: Peng Q, Li K, Han Z, Wang E, Xu Z, Liu R, Tian Y. 2013. Degradable magnesium-based implant materials with anti-inflammatory activity. J Biomed Mater Res Part A 2013:101A:1898–1906.

INTRODUCTION

The magnesium (Mg) alloys in the human body environment play an essential role as biomaterials to support the healing process of damaged organs or bone tissues.[1] In comparison with ceramics or polymeric materials, the metallic Mg materials are more suitable for load-bearing applications because of their combination of high mechanical strength and fracture toughness.[2] More significantly, the degradable product of Mg was a soluble, nontoxic oxide or hydroxide, which can temporarily enhance osteoblast activity and decrease the osteoclast number during the bone remodelling.[3] These intriguing characters have attracted great attention in terms of the development of Mg metallic implants.

At the initial development period of Mg biomaterials, some commercial Mg alloys that were used to engineer materials have been adopted to investigate as biomaterials directly, such as AZ91, AZ31, AM60B, and WE43.[4,5] However, for these conventional Mg alloys, aluminum (Al), manganese (Mn), zirconium (Zr), and rare earth elements (RE) have been used to improve the mechanical and corrosion properties. In consequence, the biotoxicity of degradation products has been an inevitable problem for the applications of commercial Mg alloys as biomaterials. For example, an excess of ionic Al has been reported to induce dementia because it can bind to inorganic phosphate causing a lack of phosphate in the body.[6] Excessive concentration of Mn has been confirmed to cause neurotoxicity, leading to Parkinson's disease.[7] The abundance of Zr is closely associated with liver, lung, breast, and nasopharyngeal cancers.[8] The phenomenon of RE enrichment in some organs and the existence of critical concentration in cell coculture experiments have been verified, although the detailed toxic mechanisms are still unclear.[9]

Therefore, the guideline that the alloying elements exist in the human body or have been clearly known the metabolism pathway has been proposed to minimize the cytotoxicity recently. On the basis of the above guideline, a series of new alloys have been developed. It has been reported that hydrogen evolution was rarely observed during the corrosion process in Mg-Zn-Ca metallic glasses implants.[10] Furthermore, Mg-6 wt % Zn alloy have been reported that it exhibited suitable mechanical strength, good

Correspondence to: Q. Peng; e-mail: pengqiuming@gmail.com
Contract grant sponsor: National Natural Science Foundation of China; contract grant number: 51101142 and 50821001
Contract grant sponsor: Postdoctoral Science Foundation; contract grant number: 2012M510766
Contract grant sponsor: Science Foundation for the Excellent Youth Scholars of Hebei Province; contract grant number: Y2012019

biocompatibility, and moderate degradation rate.[11] In addition, Mg-1 wt % Ca alloy has also been regarded as one of the promising orthopedic biodegradable materials.[12] More attractively, the binary Mg-RE (RE: Y, Gd and Dy) alloys were introduced as a novel biomaterial for fine implants or degradation stent.[13] Compared with conventional Mg alloys, the strength and corrosion resistance have been improved and they provide more attractive characteristics to develop Mg-based implants in the future. However, the alloys were mainly composed of metallic glasses or large size grains, which exhibited low deformability. In addition, as far as stents were concerned, they tended to cause injury to the blood vessels, resulting in neointimal proliferation, known as restenosis, continue to hamper initial procedural success in 10–50% of patients undergoing coronary intervention.[14] Consequently, the development of anti-inflammatory Mg-based implant material has been an interesting issue. It can substitute the drug-coating implants, which only provide temporary protection.

Silver (Ag) was added as both a grain refiner and an anti-inflammatory core. On the one hand, the refined grain can improve the mechanical strength and deformability.[15] On the other hand, silver ion is one of effective broad spectrum range of antimicrobial activity. For instance, the cream containing silver has been found as therapeutic potential for topical treatment of inflammatory skin diseases.[16] The anti-inflammatory effect of silver-polyvinyl pyrrolidone nanoparticle in *Chlamydia trachomatis*–infected macrophages and HeLa cell has been confirmed.[17] In this work, Mg-Zn-Ag–based alloys have been developed as anti-inflammatory biomaterials. The mechanical properties are improved by extrusion technology. Microstructure, mechanical and degradation properties, cytocompatibility, and anti-inflammatory activity have been investigated. The anti-inflammatory and strengthening mechanisms have been discussed.

MATERIALS AND METHODS

Materials Preparation

The nominal four Mg-1Zn-*x*Ag ($x = 0$, 0.2, 0.5, and 0.8 wt %; all compositions given thereafter in wt %) alloys have been prepared by zone solidification technology. This technology and its purifying mechanism have been reported in our previous work.[18] The alloys have been prepared in a tantalum (Ta) crucible under the protection by a mixture of CO_2 and SF_6. After mixing at 720°C for 1 h, the alloy was cast to a mould preheated at 600°C. The filled mould was held at 670°C for 1 h under the protective gas. Then, the whole steel crucible with the alloy was immersed in cool water at 30 mm/s. When the bottom of Ta crucible touched the water, it stopped for 2 s. As soon as the liquid level of inside melt was alignment with the height of outside water, the solidification process was finished. The diameter and length of ingot were 60 and 180 mm, respectively.

The solid solution treatment has been preformed at 450°C for 10 h, and then it was quenched in hot water (60°C). The ingot was preheated at 370°C for 1 h and then it was extruded immediately. The extruded temperature and extruded ratio were 370°C and 36, respectively. After extrusion, the samples of 10 mm in diameter were heated at 150°C for 30 min to eliminate the residual stress. The chemical composition of the alloys was measured by x-ray fluorescence spectroscopy (PW2400, Philip). The detailed chemical concentrations of four alloys are Mg-0.89Zn, Mg-0.82Zn-0.21Ag, Mg-0.85Zn-0.47Ag, and Mg-0.91Zn-0.79Ag.

TABLE I. Reagents for Preparation of SBF (pH 7.25, 1 L)

Adding Turn	Reagent	Amount
1	NaCl	7.996 g
2	$NaHCO_3$	0.350 g
3	KCl	0.224 g
4	$K_2HPO_4{\cdot}3H_2O$	0.228 g
5	$MgCl_2{\cdot}6H_2O$	0.305 g
6	12 mol/L HCl	40 cm^3
7	$CaCl_2$	0.278 g
8	Na_2SO_4	0.071 g
9	$(CH_2OH)_3CNH_2$	6.057 g
10	12 mol/L HCl	(about 5 mL)

Microstructure characterization

Microstructural investigations were performed using optical microscopy (OM; AMPLIVAL, Zeiss) and scanning electron microscopy (SEM; S-4700, HITACHI) equipped with energy dispersive x-ray spectrometry. For OM analysis, the standard metallographic procedures were applied, including grinding, polishing, and etching. The samples were etched in 10% picral-acetic solution (Kermel, China) to reveal grain boundaries. The grain sizes were measured using the linear intercept method.

Mechanical properties

The hardness was measured by Vickers hardness tester (Hv, HM-113, Japan); the test load and the dwelling time were 100 g and 15 s, respectively. The 5×5 matrix has been performed to measure the hardness of the alloys. The tensile and compressive tests were performed using mechanical testing machine (WAW-1000, ZWICK) at room temperature with an initial strain rate of 1.7×10^{-3} s^{-1}. The extruded samples were machined into 3.5 mm in diameter and the gauge length of 30 mm for tensile test. The diameter and the height of compression samples were 4 and 8 mm, respectively. Five duplicate samples have been performed to evaluate the mechanical properties of the alloys.

Degradation properties

In vitro degradation with immersion tests. The degradation rate was tested in simulated body fluid (SBF) at room temperature according to ASTM-G31-72 (the ratio of surface area to solution volume was 1 cm^2:20 mL).[19] The detailed composition and preparation method of SBF are shown in Table I. Both the diameter and the height of tested samples were 10 mm. The tested time is 2 weeks. The degradation rate was determined according to three parallel tests. The corrosion reaction of Mg-based alloys was calculated by the following chemical equation[20]:

$$Mg + 2H_2O = Mg(OH)_2 + H_2 \uparrow$$

After immersion, the corrosion rate was cross-checked by measuring the weight of the specimens before and after the immersion test in SBF. The latter was performed after cleaning and removal of all corrosion products in chromic acid (Kermel, China) according to the ASTM-G31-72 (180 g/L, 20 min immersion at room temperature).[19] The average corrosion rate (P_i, mm/y) is given:

$$P_i = (K \times W)/(A \times T \times D) \quad (1)$$

where the coefficient $K = 8.76 \times 10^4$, W is the weight loss (g), A is the sample area exposed to solution (cm^2), T is the exposure time (h), and D is the density of the material (g/cm^3).

In vitro degradation with electrochemical tests. Electrochemical tests were performed using potentiostat/frequency response analysis system (VSP, Bio-logic) to evaluate the corrosion behavior of the specimens. At least three times were repeated to obtain consistent electrochemical behavior. Saturated Ag/AgCl (saturated with KCl) was used as the reference electrode. A platinum mesh and the investigated specimen were used as the counter electrode and the working electrode (0.5 cm^2 exposed area), respectively. The electrochemical tests were conducted in SBF solution. Potentiodynamic polarization tests were performed at a scan rate of 0.5 mV/s and a final anodic current density of 0.1 mA/cm^2 after an initial 0.5-h exposure to the test electrolyte for achieving a stabilized open circuit potential. The polarization curves were used to estimate the corrosion current density (i_{corr}) at corrosion potential (E_{corr}) by Tafel extrapolation of the cathodic branch according to ASTM-G102-89.[21] The corrosion rate (P_i) can be calculated using the conversion equation[22]:

$$P_i = 22.85 i_{corr}. \quad (2)$$

Electrochemical impedance spectroscopy (EIS) studies were performed at open circuit potential with the amplitude of 10 mV over the frequency range of 10.000–0.1 Hz on specimens exposed to the corrosive electrolyte for different durations, viz., 1, 2, 6, 9, and 12 h to understand the degradation mechanism. All electrochemical tests were performed at room temperature with stirring in the bottom, and the tests were performed in triplicate to ascertain reproducibility.

Cytocompatibility

HeLa cervical carcinoma cells were cultured in Dulbecco's modified eagle's medium (DMEM), supplemented with 10% fetal bovine serum (FBS) in a humidified incubator at 95% relative humidity and 5% CO_2 at 37°C. Cytotoxicity was determined by indirect contact using Mg-1Zn-0.8Ag alloy. Extracts were prepared according to ISO 10993-5.[21] In brief, the extraction media were serially diluted to 50 and 10% concentration after 72 h incubation in a humidified atmosphere with 5% CO_2 at 37°C. The DMEM medium acted as a negative control, whereas DMEM medium containing 0.64% phenol as a positive control. Cells were incubated in 96-well flat-bottomed cell culture plates at 2.5×10^4 cells/ml medium in each well and incubated for 24 h to allow cell attachment. Then, the medium was replaced by 200 μL extraction medium. After incubation in a humidified atmosphere for 24, 48, and 72 h, cell morphology was observed by OM. 3-(4,5-dimethylthiazol-2-yl)-2,5-diphenyltetrazolium bromide (MTT) was then dissolved in phosphate-buffered saline at a concentration of 5 mg/mL. After that, 20 μL MTT was added to each well, and the samples were incubated for 4 h (37°C, 5% CO_2, 95% relative humidity). Subsequently, the formazan product was solubilized by addition of 150 μL of dimethyl sulfoxide, and optical density (OD) measurements were conducted at 490 nm using a Wellscan MK3 spectrophotometer (Labsystem). The cell relative growth rate (RGR) was calculated according to the following formula:

$$\mathrm{RGR} = \mathrm{OD}_{\mathrm{test}}/\mathrm{OD}_{\mathrm{negative}} \times 100\% \quad (3)$$

Anti-inflammatory function

Anti-inflammatory assay with interleukin-1α. Mg-1Zn-0.8Ag alloy was immersed in SBF liquid at room temperature for 24 h. The dimension of sample was $1 \times 1 \times 1$ mm^3. The volume of SBF liquid was 1 L. The concentration of Ag ion (0.005 mg/L) was measured by chemical titration method. For the assays, the samples were diluted in Hank's solution to silver ion of 1×10^{-4}, 1×10^{-3}, 2×10^{-3}, and 3×10^{-3} mg/l. The DMEM medium containing Mg-1Zn alloy (0.006 mg/L Zn ion) acted as a negative control, whereas DMEM medium containing 0.01% aspirin as a positive control. RAW264.7 cell was seeded at a density of 2×10^6 cells/5 mL into 25 cm^2 cell culture flasks containing medium with 5% FBS and cultured overnight. The medium was exchanged and cells cultured for an additional 48 h. Then, cell numbers were determined, and culture medium was collected and centrifuged at 1000*g* for 5 min to remove any particles, and the supernatants were frozen at −80°C until used in enzyme-linked immunoassay systems (ELISA). The concentration of interleukin (IL)-1α in the supernatants per 2×10^6 cells was measured using an ELISA kit at 450 nm according to the manufacturer's protocol. The assay range is 3–100 ng/L. The concentration of IL-1α in the samples is determined by comparing the OD of the samples with the standard curve.

Anti-inflammatory assay with nitric oxide release measurements. RAW264.7 cell was transferred when the cells formed packed monolayer. A total of 10 ng/mL lipopolysaccharide (LPS; Sigma) was added to the well to stimulate the cell for 60 min. The same method as above IL-1α measurement was used to prepare the samples. The concentration of silver ion was 1×10^{-4}, 1×10^{-3}, 2×10^{-3}, and 3×10^{-3} mg/L. The DMEM medium containing Mg-1Zn alloy (0.006 mg/L ionic zinc) acted as a negative control, whereas DMEM medium containing 0.01% aspirin as a positive control. Adherent cells in 96-well plates (2×10^4 cells/well) in serum-free DMEM were treated with the samples at 37°C.

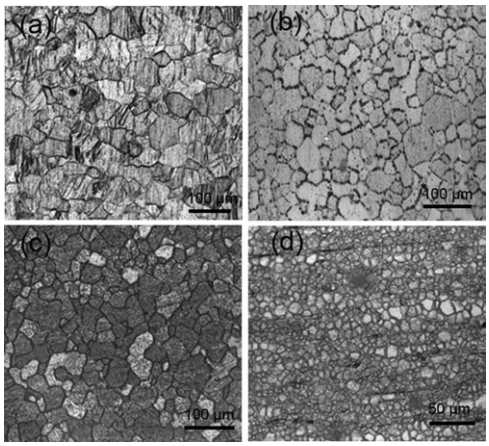

FIGURE 1. Microstructure of the extruded alloys perpendicular to the extruded direction: (a) Mg-1Zn alloy; (b) Mg-1Zn-0.2Ag alloy; (c) Mg-1Zn-0.5Ag alloy; (d) Mg-1Zn-0.8Ag alloy.

After the incubation for the indicated periods of time, nitric oxide (NO) production was determined by assaying the culture medium for NO^{2-}, the stable reaction product of NO with molecular oxygen using Griess reagent (3 m*M* sulfanilic acid, 30 m*M* *N*-1-naphtyl-ethlenediamine dihydrochloride, 25% glacial acetic acid). The supernatants of cultured cells were mixed with twice volume of Griess reagent. After incubation at room temperature for 20 min, the absorbance at 550 nm was then measured using Wellscan MK3 spectrophotometer according to the manufacturer's protocol. The NO^{2-} concentrations were estimated from a reference to a standard curve for serial twofold dilution of $NaNO_2$.

Statistical analysis

At least three parallel experiments were conducted. The results were expressed as mean ± standard deviations. Statistical analysis was performed by one-way analysis of variance, and the differences between the means were tasted using Duncan's multiple range tests. *P* values of less than 0.05 were considered statistically significant.

RESULTS

Microstructural characterization

The microstructures of the extruded alloys perpendicular to the extrusion direction are shown in Figure 1. The alloys are mainly composed of fine grain boundaries and Mg matrix. Moreover, the width of grain boundary is increased with the increment of Ag content, which is mostly related to their reduced corrosion resistance. The grain size is decreased with the increment of Ag content (Fig. 2). The grain size of extruded Mg-1Zn alloy is 70 ± 12.5 μm, which is 3.3 times as high as that of Mg-1Zn-0.8Ag alloy. Some deformation twins formed during the polishing process are observed on the surface of Mg-1Zn alloy. Conversely, there is no deformation twins detected in the alloys containing Ag. The same trend was confirmed using SEM (Fig. 3).

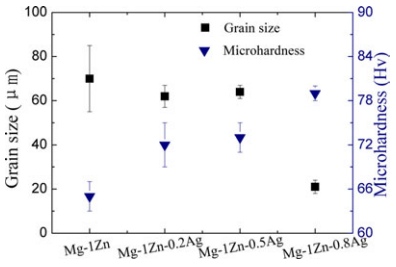

FIGURE 2. The grain size and microhardness of extruded Mg-1Zn-*x*Ag alloys. [Color figure can be viewed in the online issue, which is available at wileyonlinelibrary.com.]

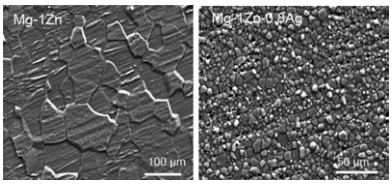

FIGURE 3. SEM microstructure of extruded Mg-1Zn and Mg-1Zn-0.8Ag alloys.

The reprehensive SEM graphs of Mg-1Zn-0.8Ag alloy after the immersion test in SBF are shown in Figure 4. The convex-shaped morphology in some areas was observed on the surface [Fig. 4(a)]. It was mainly associated with galvanic corrosion during the immersion process. In addition, some fine cracks were detected with high magnification [Fig. 4(b)], which was the released channels of hydrogen during the decomposed process. Figure 4(c–e) was the element map of O, P, and Ca in Figure 4(b). It can be found that the elements of Ca and P were aggregated on the surface.

Mechanical properties

The microhardness of extruded alloys is also shown in Figure 2. The hardness of extruded binary Mg-1Zn alloy was 65 Hv. The hardness of the alloys was improved with the increment of Ag content in the matrix. The max hardness of Mg-1Zn-0.8Ag alloy was 79 Hv, which was 1.2 times as high as that of binary Mg-1Zn alloy.

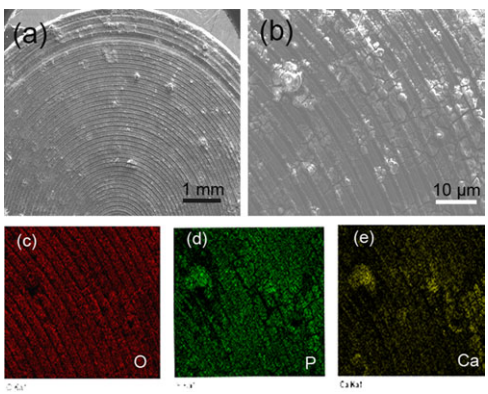

FIGURE 4. SEM graphs of Mg-1Zn-0.8Ag alloy after test IL-1α: (a) macrostructure, (b) local high magnification, (c–e) element map of O, P, and Ca in (b), respectively. [Color figure can be viewed in the online issue, which is available at wileyonlinelibrary.com.]

TABLE II. The Mechanical Properties of Extruded Alloys and Bone at Room Temperature, Including Standard Deviation in Parentheses

		Tensile properties			Compressive properties		
Alloys	Young's modulus	TYS (MPa)	UTS(MPa)	ε(%)	CYS (MPa)	UCS (MPa)	ε′ (%)
Mg-1Zn	42 (1.5)	85 (2)	190 (10)	10.1 (0.4)	71 (1)	237 (10)	14.1 (0.5)
Mg-1Zn-0.2Ag	43 (0.8)	102 (3)	201 (9)	11.8 (0.6)	93 (1)	240 (11)	15.0 (0.4)
Mg-1Zn-0.5Ag	43 (0.9)	115 (2)	207 (10)	11.5 (0.4)	111 (1)	250 (8)	18.2 (0.4)
Mg-1Zn-0.8Ag	44 (0.7)	127 (1)	209 (9)	13.6 (0.4)	122 (1)	258 (6)	19.1 (0.5)
Natural bone[1,8]	3–20	—	104–121	Brittle	—	130–180	Brittle

The tensile and compressive properties of the alloys at room temperature were summarized in Table II. The mechanical properties of natural bone (mature humeral bone) were also listed in Table II in comparison with our results. Both tensile and compressive tests show the same trend with increasing Ag content. The yield strength (YS) and ultimate strength are improved by adding alloying element of Ag. Mg-1Zn-0.8Ag alloy exhibits the highest mechanical properties. The value of tensile YS, ultimate tensile strength (UTS), and fracture elongation (ε) at room temperature is 127 MPa, 209 MPa, and 13.6%, respectively. The value of compressive YS, ultimate compressive strength, and fracture elongation (ε') at room temperature are 122 MPa, 258 MPa, and 19.1%, respectively. The alloys reveal higher ductility than natural bone because the bone is mostly composed of porous brittle biomaterials.[8]

Degradation properties

The corrosion behavior of the specimens evaluated by potentiodynamic polarization after 2 h of exposure in SBF solution is shown in Figure 5. The i_{corr} was increased significantly with the increment of Ag content. Mg-1Zn alloy exhibits lowest $i_{corr,}$ and the other three alloys containing Ag show the same order of magnitude in SBF solution. The i_{corr} ($1.63 \pm 0.05 \times 10^{-2}$ mA/cm^2) of Mg-1Zn-0.8Ag alloy is about eight times as high as that ($-2.21 \pm 0.02 \times 10^{-1}$ mA/cm^2) of Mg-1Zn alloy. At the same time, the obvious platforms were observed in Mg-1Zn, Mg-1Zn-0.2Ag, and Mg-1Zn-0.5Ag alloys. With the increment of Ag content, the platform became more and more indistinct. The E_{pp} has hardly been detected in Mg-1Zn-0.8Ag alloy. With increasing the concentration of Ag, the segregation area of Ag in the matrix is increased correspondingly. Thereafter, it is prone to form pitting corrosion, which can breakdown the oxide film readily. The solution can penetrate the film and decompose the alloy continuously. As a result, the passivation behavior cannot be observed in Mg-1Zn-0.8Ag alloy.

The corrosion rate of the alloys is determined by weight loss and Tafel curves. The detailed results are shown in Figure 6. The consistent trend that the corrosion rate is increased with increasing the content of Ag is observed by the use of two methods. The Mg-1Zn alloy exhibits the best anticorrosion properties based on both weight loss method and Tafel curve. The average corrosion rate of Mg-1Zn, Mg-1Zn-0.2Ag, Mg-1Zn-0.5Ag, and Mg-1Zn-0.8Ag alloys calculated by Tafel curve is 0.7 ± 0.06, 2.8 ± 0.09, 3.4 ± 0.11, and 3.7 ± 0.12 mm/y, respectively. The average values determined by weight loss are obviously higher than those calculated by Tafel curves. The corresponding corrosion rate of four investigated alloys is 1.7 ± 0.41, 3.8 ± 0.52, 4.9 ± 0.55, and 6.3 ± 0.62 mm/y, respectively. This error is mainly introduced during the washing process of corroded products. Specifically, the matrix containing higher Ag content is more prone to be corroded readily in chromic acid liquid.

Cytocompatibility

Figure 7 shows the RGR values of extruded Mg-1Zn-*x*Ag alloys, including HeLa cell after incubation for 24, 48, and 72 h. With increasing the incubation time, the RGR values are fluctuated slightly. The gap between the investigated samples and the negative one is small ($^*p > 0.05$). On the contrary, the difference between the investigated samples and the positive one is obvious ($^{**}p < 0.01$). It is demonstrated that Mg-Zn-Ag alloys exhibit good cytocompatibility.

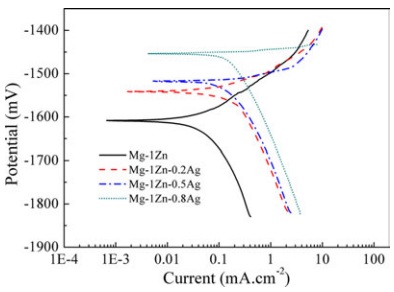

FIGURE 5. Potentiodynamic polarization curves of the alloys in SBF (after 2 h of exposure). [Color figure can be viewed in the online issue, which is available at wileyonlinelibrary.com.]

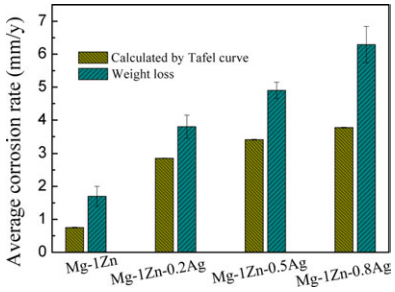

FIGURE 6. Corrosion rate of extruded alloys in SBF at room temperature. [Color figure can be viewed in the online issue, which is available at wileyonlinelibrary.com.]

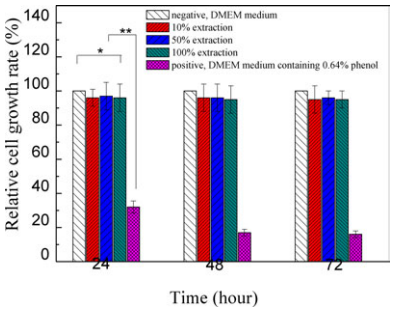

FIGURE 7. Relative cell growth rate (HeLa cell) in solution containing Mg-1Zn-0.8Ag alloy after different incubation time. The assays data are expressed as means ± standard deviations ($n = 5$),*$p > 0.05$, **$p < 0.01$. [Color figure can be viewed in the online issue, which is available at wileyonlinelibrary.com.]

The representative cell morphologies containing Mg-1Zn-0.8Ag alloy and reference well (DMEM medium) were observed after different culturing time (Fig. 8). The amount of adhered cell in reference well is higher than that containing 100% extraction. After incubating for 72 h, the sphere-shaped cell in reference well is increased significantly. It is mainly because that the adhered cell grows rapidly, leading some cells are isolated from the container. For 100% extraction sample, the adhered dendrite-shaped cells started to proliferate after 72-h incubation [Fig. 8(f)].

Anti-inflammatory activity

The concentration of IL-1α in the solution including RAW264.7 cell is shown in Figure 9. Compared with the negative sample (Mg-Zn), the same values are observed when the content of Ag is below 1×10^{-3} mg/L (*$p >$ 0.05). However, when the concentration of Ag is higher than 2×10^{-3} mg/L, the distinct anti-inflammatory activity has been detected (**$p < 0.05$). At the same time, it reveals that the anti-inflammatory activity directly depends on the concentration of Ag in solution.

The released NO in the solution after adding RAW264.7 cell is shown in Figure 10. The same trend was observed as that of IL-1α. Namely, the concentration of NO was decreased with the increment of Ag content. The only difference lies in higher critical concentration of Ag. When the concentration of Ag is higher than 2×10^{-3} mg/L, the obvious anti-inflammatory effect was obtained (**$p < 0.01$).

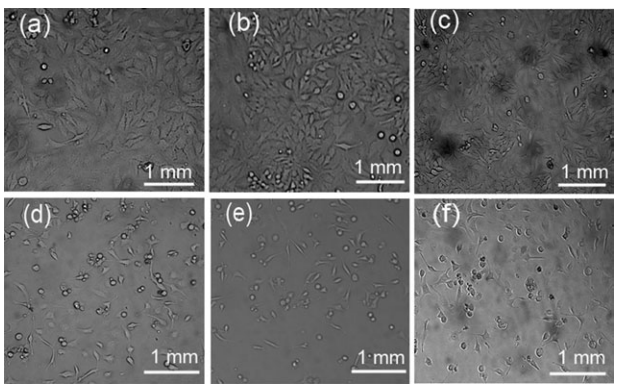

FIGURE 8. Cell morphology of different wells after different incubation time, reference well (DMEM medium): 24 h (a), 48 h (b), and 72 h(c); 100% extraction sample: 24 h (d), 48 h (e), and 72 h (f).

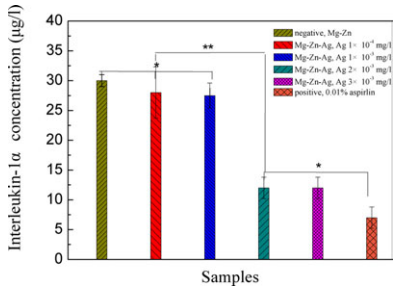

FIGURE 9. The concentrations of interleukin-1α (RAW264.7 cell) after adding different alloys. The assays data are expressed as means ± standard deviations ($n = 3$) *$p > 0.05$, **$p < 0.01$. [Color figure can be viewed in the online issue, which is available at wileyonlinelibrary.com.]

DISCUSSION

In contrast to the extruded Mg-1Zn alloy, the mechanical properties are improved significantly with the addition of Ag element. Especially, the extruded Mg-1Zn-0.8Ag alloy shows a good combination of strength and ductility. The improved mechanical properties of the Mg-1Zn-*x*Ag alloys are related to the fine grain strengthening, which forms due to the recrystallization. In general, the recrystallization process is driven by the stored energy of deformation in the form of grain boundaries. During the extrusion, the grains are not stable and the grain growth readily occurs. It is well known that grain growth is divided into two types, normal grain growth and abnormal grain growth (secondary recrystallization). Moreover, the driving pressure for grain growth is often some two orders of magnitude less than that for recrystallization.[23] Consequently, at a particular temperature, grain boundary velocities will be slower than during recrystallization and boundary migration will be much more affected by the pinning effects of solutes. In our system, Zn and Ag are well distributed in the Mg matrix because of the high solubility (max. solubility: Zn, 6.2 wt %, 350°C; Ag, 15.02 wt %, 472°C).[24] Thus, the recrystallization behavior plays a prior role on grain size rather than the grain

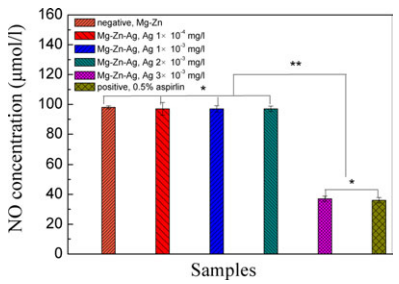

FIGURE 10. The concentrations of released nitrogen oxide (RAW264.7 cell) after adding different alloys. The assays data are expressed as means ± standard deviations ($n = 3$),*$p > 0.05$, **$p < 0.01$. [Color figure can be viewed in the online issue, which is available at wileyonlinelibrary.com.]

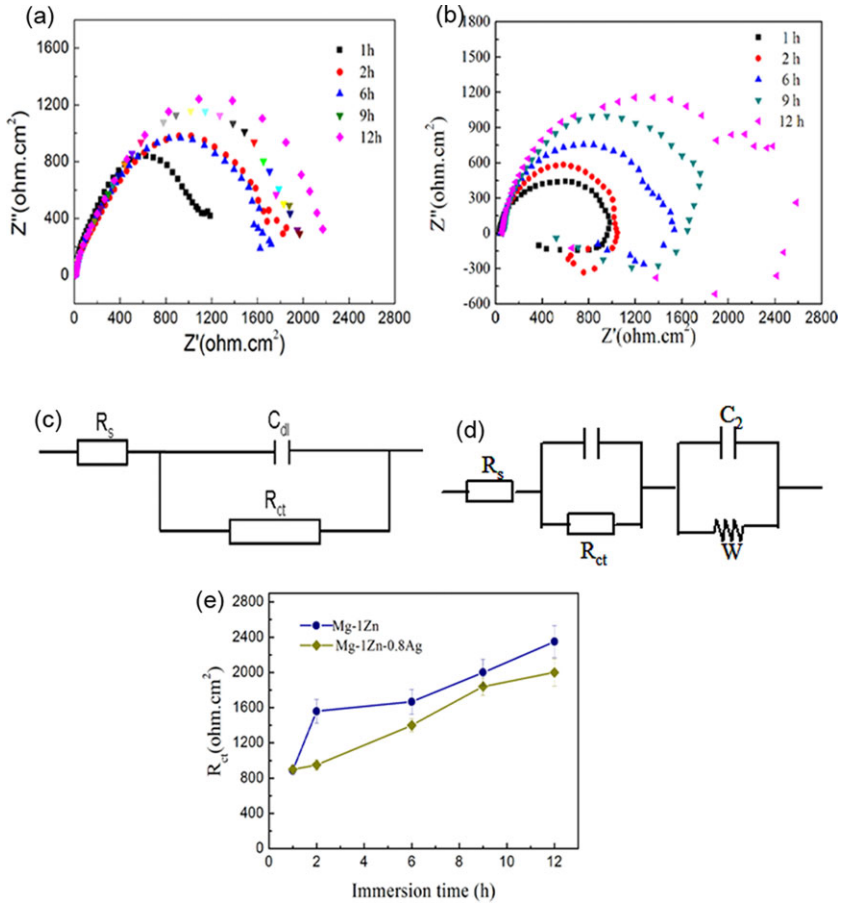

FIGURE 11. Electrochemical measurement in SBF at 37 ± 2°C: (a) Nyquist plots of Mg-1Zn alloy; (b) Nyquist plots of Mg-1Zn-0.8Ag alloy; (c) the equivalent circuit of Mg-1Zn alloy fitting Nyquist plots; (d) the equivalent circuit of Mg-1Zn-0.8Ag alloy fitting Nyquist plots; (e) the relationship between R_{ct} and the different immersion time. [Color figure can be viewed in the online issue, which is available at wileyonlinelibrary.com.]

growth. Therefore, the grain size is decreased after extrusion. Moreover, this effect is increased with increasing the concentration of Ag. This explanation is confirmed by microstructure observation (Fig. 2).

In addition, the corrosion deterioration of the specimens in corrosive electrolytes with prolonged immersion time up to 12 h was examined by EIS measurements (Fig. 11). For Mg-1Zn alloy, the EIS curves chiefly conclude a capacitive loop in high-frequency (HF) region and an inductive loop at low-frequency region (LF). On the contrary, the EIS curves of Mg-1Zn-0.8Ag alloy are mostly composed of two capacitive loops (HF and LF) and an inductive loop (LF). According to previous relevant studies,[25] it is well known that the inductive loop in LF region can be ascribed to the partially protective film on the surface of Mg-based alloys. Therefore, the approximate equivalent circuit [Fig. 11(c–d)] for Mg-1Zn and Mg-1Zn-0.8Ag alloys can be denoted as $R_S(C_{dl}R_{ct})$ and $R_S(C_{dl}R_{ct})$ (C_2R_w), respectively. R_S and R_{ct} are SBF solution resistance and charge transfer resistance, respectively. R_w is inductive resistance. C_{dl} and C_2 are electric double-layer capacitor and electric inductive capacitor, respectively. The relationship between R_{ct} and immersion time fitting from Nyquist plots is shown in Fig. 11(e). It can be found that R_{ct} is increased when retarding the immersion time in SBF. A wide platform is observed during corrosion process in Mg-1Zn alloy. However, R_{ct} of Mg-1Zn-0.8Ag alloy is increased with increasing the immersion time continuously. It is consistent with the above results. Namely, the corrosion rate was enhanced with increasing Ag concentration.[26]

However, it should be mentioned that the suitable corrosion rate is crucial to retain the constant concentration of silver ion in the neighboring environment of implants, which is of benefit for the high anti-inflammatory activity. It is because that the antibacterial effect does not result from the alloy containing silver, but rather the silver ion. The standard electrode potential of Mg, Zn, and Ag is −2.37, −0.763, and 0.7995 V.[27] Therefore, when Ag and Zn are added into Mg matrix, the micro galvanic cell can form readily in the SBF. On the one hand, the oxidized layer on the surface is too loose to prevent the further corrosion. Thus, the SBF can penetrate the oxidized layer and the alloys will be decomposed gradually. On the other hand, the amount of oxides is increased progressively owing to the low solubility of decomposed products in SBF, resulting in the increment of R_{ct} of interface finally [Fig. 11(d)]. Thus, the mechanical integrity can be compensated by improved mechanical

properties and thickness, although the addition of Ag increases the corrosion rate.

Mg-1Zn-0.8Ag alloy exhibits not only high mechanical properties but also good cytocompatibility (**$p < 0.01$). The RGR results of HeLa cell reveal that the decomposed products of Mg-1Zn-0.8Ag system are harmless. It is well known that both Mg and Zn are the important elements in our daily life. It is necessary to intake foods containing trace Mg and Zn to avoid the metabolism deficiencies. The high biocompatibility of Mg and Zn has also been reported in Mg-Zn binary alloys.[28] Especially, it has reported that even though the 100% extraction of decomposed products in Mg-6 wt % Zn alloys was acceptable for L-929 cell, silver's antimicrobial activity has been attributed to its affinity for binding and inactivating critical negatively charged functional groups in cells.[29] However, the biocompatibility of silver ion was correlated with the concentration of released ions.[30] For example, it was reported that the structure of Ag^+-implanted pyrolytic carbon is maintaining the original biocompatibility when the ion dose is not exceeding 1×10^{16} ions/cm^2.[31] In addition, the World Health Organization (1996) permits maximal concentration of 0.1 mg/L of Ag ions in drinking water disinfection.[32] In our investigations, Mg-Zn-Ag alloys with optimal degradation rate can be deemed as a reservoir that effectively prevents the silver ion concentration reaching cytotoxic level for cells.

Finally, both IL-1α and NO models show the silver ion was closely related to the anti-inflammatory role. Meanwhile, the same trend that the anti-inflammatory effect was improved with the increased silver ion concentration in solution, although the critical values were different. It can be confirmed that the anti-inflammation effect becomes obvious when the content of Ag was higher than 2×10^{-3} mg/L. On the basis of previous results,[33–35] it can be found that silver is a powerful antimicrobial agent used to control infection of the eyes, burns, and acute and chronic wounds. In these investigations, the new application of antibacterial properties has been confirmed. The similar attempt has been reported recently[36] that a 3D-glass-ceramic scaffold for bone tissue engineering with an interconnected macroporous network of pores have successfully doped with silver ion to confer antibacterial properties. Compared with simple silver implantation coating, the silver element plays multiple functions in our designed alloys. Namely, the silver addition becomes the core determining the mechanical properties, corrosion rate, cytocompatibility, and anti-inflammatory ability.

CONCLUSION

Taken together, our data indicate that extruded Mg-Zn-Ag system displays improved mechanical properties, good cytocompatibility, and anti-inflammatory activity, which is beneficial to healing injured tissue and to decreasing postoperative inflammation simultaneously. The enhanced mechanical properties are mainly associated with fine grain size. *In vitro* test reveals that the high cytocompatibility stems form the moderate degradation rate of alloys. The IL-1α and NO modes exhibit that the products containing the silver ion are attributed to the anti-inflammatory activity. Furthermore, a controlled and sustained release of silver ion by the use of Mg-Zn-Ag biomaterial offers a balance between cytocompatibility and anti-inflammatory effect. It can be confirmed that it is promising to develop a new biodegradable metallic implant to eliminate restenosis causing by neointima trauma.

ACKNOWLEDGMENTS

The authors thank Ms. Li Hui for her valuable technical assistance.

REFERENCES

1. Staiger M, Pietak A, Huadmai J, Dias G. Magnesium and its alloys as orthopedic biomaterials: A review. Biomaterials 2006;27:1728–1734.
2. Serre C, Papillard M, Chavassieux P, Boivin G. In vitro induction of a calcifying matrix by biomaterials constituted of collagen and hydroxyapatite: An ultrastructural comparison of three types of biomaterials. Biomaterials 1993;14:97–106.
3. Janning C, Willbold E, Vogt C, Nellesen J, Meyer-Lindenberg A, Windhagen H, Thorey F, Witte F. Magnesium hydroxide temporarily enhancing osteoblast activity and decreasing the osteoclast number in peri-implant bone remodelling. Acta Biomater 2010;6:1861–1868.
4. Wiedmann-Al-Ahmad M, Gutwald R, Lauer G, Hübner U, Schmelzeisen R. How to optimize seeding and culturing of human osteoblast-like cells on various biomaterials. Biomaterials 2002;23:3319–3328.
5. Witte F, Hort N, Vogt C, Cohen S, Kainer K, Willumeit R, Feyerabend F. Degradable biomaterials based on magnesium corrosion. Curr Opin Sol State Mater Sci 2008;12:63–72.
6. Shaw C, Petrik M. Aluminum hydroxide injections lead to motor deficits and motor neuron degeneration. J Inorg Biochem 2009;103:1555–1562.
7. Aschner M, Schneider T, Zheng J. Manganese: Recent advances in understanding its transport and neurotoxicity. Toxicol Appl Pharmacol 2007;221:131–147.
8. Gibson L, Ashby M. Cellular Solids: Structure and Properties. Sydney: Pergamon; 1988.
9. Feyerabend F, Fischer J, Holtz J, Witte F, Willumeit R, Drücker H, Vogt C, Hort N. Evaluation of short-term effects of rare earth and other elements used in magnesium alloys on primary cells and cell lines. Acta Biomater 2010;6:1834–1842.
10. Zberg B, Uggowitzer P, Loffler J. MgZnCa glasses without clinically observable hydrogen evolution for biodegradable implants. Nat Mater 2009;8:887–891.
11. Zhang S, Zhang X, Zhao C, Li J, Song Y, Xie C, Tao H, Zhang Y, He Y, Jiang Y, Bian Y. Research on an Mg-Zn alloy as a degradable biomaterial. Acta Biomater 2010;6:626–640.
12. Li Z, Gu X, Lou S, Zheng Y. The development of binary Mg-Ca alloys for use as biodegradable materials within bone. Biomaterials 2008;29:1329–1344.
13. Hort N, Huang Y, Fechner D, Störmer M, Blawert C, Witte F, Vogt C, Drücker H, Willumeit R, Kainer KU, Feyerabend F. Magnesium alloys as implant materials—Principles of property design for Mg-RE alloys. Acta Biomater 2010;6:1714–1725.
14. Acharya G, Park K. Mechanisms of controlled drug release from drug-eluting stents. Adv Drug Del Rev 2006;58:387–401.
15. Hanzi A, Dalla Torre F, Sologubenko A, Gunde P, Schmid-Fetzer R, Kuehlein M, Loffler J, Uggowitzer P. Design strategy for microalloyed ultra-ductile magnesium alloys. Phil Mag Lett 2009;89:377–390.
16. Bhol K, Alroy J, Schechter P. Anti-inflammatory effect of topical nanocrystalline silver cream on allergic contact dermatitis in a guinea pig model. Clin Exp Dermatol 2004;29:282–287.
17. Yilma A, Singh S, Murtada T, Fairley S, Subbarayan P, Dennis V. Evidence of the anti-inflammatory effect of silver-polyvinyl pyrrolidone nanoparticles (Ag-PVP) in chlamydia trachomatis infected macrophages and HeLa cells. Nanotech 2011;3:447–450.

18. Peng Q, Huang Y, Zhou L, Hort N, Kainer KU. Preparation and properties of high purity Mg-Y biomaterials. Biomaterials 2010;31: 398–403.
19. ASTM-G31–72. American Society for Testing and Materials: Standard Practice for Laboratory Immersion Corrosion Testing of Metals. Philadelphia, PA; 2004.
20. Song G, Atrens A. Understanding magnesium corrosion—A framework for improved alloy performance. Adv Eng Mater 2003; 5:837–858.
21. ASTM-G102–89. American Society for Testing and Materials: Standard Practice for Calculation for Corrosion Rates and Related Information from Electrochemical Measurements. Philadelphia, PA; 1999.
22. Zhao M, Liu M, Song G, Atrens A. Influence of pH and chloride ion concentration on the corrosion of Mg alloy ZE41. Corr Sci 2008;50:3168–3178.
23. Rollett A, Humphreys F, Hatherly M. Recrystallization and Related Annealing Phenomena. Pergamon: Oxford; 2004.
24. Avedesian M, Baker H. Handbook: Magnesium and Magnesium Alloys. Materials Park, OH: ASM International; 1999.
25. Song G. Recent progress in corrosion and protection of magnesium alloys. Adv Eng Mater 2005;7:563–586.
26. Na Y, Eliezer D, Shin K. Corrosion of new wrought magnesium alloys. Mater Sci Forum 2005;488–489:839–844.
27. Milazzo G, Caroli S, Sharma V. Tables of Standard Electrode Potentials. Chichester: Wiley; 1978.
28. Li J, Song Y, Zhang S, Zhao C, Zhang F, Zhang X, Cao L, Fan Q, Tang T. In vitro responses of human bone marrow stromal cells to a fluoridated hydroxyapatite coated biodegradable Mg-Zn alloy. Biomaterials 2010;31:5782–5788.
29. Atiyeh B, Costagliola M, Hayek S, Dibo S. Effect of silver on burn wound infection control and healing: Review of the literature. Burns 2007;33:139–148.
30. Maria CC, Mónica Fernández L de M, Ana MC. Metallic dental material biocompatibility in osteoblast-like cells: Correlation with metal ion release. Biol Trace Elem Res 2004;100:151–168.
31. Tang H, Liu T, Liu X, Gu H, Zhao J. A study on biocompatibility and bactericidal properties of pyrolytic carbon by silver ion implantation. Nucl Instrum Meth B 2007;255:304–308.
32. Pelkonen K, Heinonen-Tanski H, Hanninen O. Accumulation of silver from drinking water into cerebellum and musculus soleus in mice. Toxicology 2003;186:151–157.
33. Granchi D, Stea S, Ciapetti G, Savarino L, Cavedagna D, Pizzoferrato A. In vitro effects of bone cements on the cell cycle of osteoblast-like cells. Biomaterials 1995;16:1187–1192.
34. Ferreira M, Pereira M, Costa F, Sousa J, Simões de Carvalho G. Comparative study of metallic biomaterials toxicity: A histochemical and immunohistochemical demonstration in mouse spleen. J Trace Elem Med Bio 2003;17:45–49.
35. Declercq H, Verbeeck R, De Ridder L, Schacht E, Cornelissen M. Calcification as an indicator of osteoinductive capacity of biomaterials in osteoblastic cell cultures. Biomaterials 2005;26:4964–4974.
36. Balagna C, Vitale-Brovarone C, Miola M, Verné E, Canuto R, Saracino S, Muzio G, Fucale G, Main G. Biocompatibility and antibacterial effect of silver doped 3D-glass-ceramic scaffolds for bone grafting. J Biomater Appl 2011;6:596–617.